Published in final edited form as:
Proc SPIE Int Soc Opt Eng. 2016 February 27; 9788: . doi:10.1117/12.2216418.

Respiration gating and Bloch fitting improve pH measurements with acidoCEST MRI in an ovarian orthotopic tumor model

Kyle M Jones[a], **Edward A Randtke**[b], **Christine M Howison**[b], and **Mark D Pagel**[a,b,c]

[a]Biomedical Engineering, University of Arizona, Tucson, AZ

[b]Department of Medical Imaging, University of Arizona, Tucson, AZ; Cancer Biology Program

[c]University of Arizona Cancer Center, Tucson, AZ

Abstract

We have developed a MRI method that can measure extracellular pH in tumor tissues, known as acidoCEST MRI. This method relies on the detection of Chemical Exchange Saturation Transfer (CEST) of iopamidol, an FDA-approved CT contrast agent that has two CEST signals. A $\log_{10}$ ratio of the two CEST signals is linearly correlated with pH, but independent of agent concentration, endogenous T_1 relaxation time, and B_1 inhomogeneity. Therefore, detecting both CEST effects of iopamidol during *in vivo* studies can be used to accurately measure the extracellular pH in tumor tissues. Past *in vivo* studies using acidoCEST MRI have suffered from respiration artifacts in orthotopic and lung tumor models that have corrupted pH measurements. In addition, the non-linear fitting method used to analyze results is unreliable as it is subject to over-fitting especially with noisy CEST spectra. To improve the technique, we have recently developed a respiration gated CEST MRI pulse sequence that has greatly reduced motion artifacts, and we have included both a prescan and post scan to remove endogenous CEST effects. In addition, we fit the results by parameterizing the contrast of the exogenous agent with respect to pH via the Bloch equations modified for chemical exchange, which is less subject to over-fitting than the non-linear method. These advances in the acidoCEST MRI technique and analysis methods have made pH measurements more reliable, especially in areas of the body subject to respiratory motion.

Keywords

CEST MRI; pH; Bloch fitting; respiration gating; cancer

1. INTRODUCTION

Cancer cells prefer to produce energy through anaerobic glycolysis rather than oxidative phosphorylation.[1] As a result, tumors typically have a lower extracellular pH (pHe) environment than healthy tissue due to excess lactic acid buildup, which can be toxic to nearby tissue and also lead to metastasis.[2–4] Thus, measuring pHe has potential to characterize tumor aggressiveness since more metabolically active tumors will produce more lactic acid than indolent or benign tumors.

Some chemotherapies can be weak acid or weak base drugs. Weak base drugs like doxorubicin (AdriamycinVR, Pfizer Inc., New York, NY) may exhibit lower therapeutic efficacy than weak acid drugs like esomeprazole (NexiumTM, AstraZeneca plc, London UK) against highly acidic tumors.[5–8] Therefore, measuring tumor pHe has the potential to predict therapeutic efficacy of a weak base drug or weak acid drug before the therapeutic treatment is initiated for each patient. In addition, treatments that alkalinize the tumor microenvironment, such as sodium bicarbonate, may decrease the likelihood of tumor metastasis as well as increase the effectiveness of weak base drugs.[9] Accurately monitoring pHe in tumor as well as normal tissue may aid in evaluating if an alkalinizing treatment should be used and the amount to be used so that the dose remains non-toxic to healthy tissue.

Our group has shown success in measuring tumor pHe with chemical exchange saturation transfer (CEST) MRI, a noninvasive imaging method that saturates exchangeable protons with a MR radio frequency pulse.[10] Since this CEST MRI technique measures the level of acidity in a tissue, we have termed it acidoCEST MRI. To measure tumor pHe, we have used iopamidol (Isovue™, Bracco Imaging, Inc.), a clinically approved X-ray/CT iodinated contrast agent.[11] Because iopamidol is a highly polar chemical agent, it remains in the extracellular space during the time frame of an MRI study making pH measurements truly extracellular. Iopamidol possesses two exchangeable amide protons that can each be selectively saturated. Additionally, the exchange rates of these labile protons are pH-dependent because chemical exchange of an amide group is base-catalyzed.[12] We have previously shown that a $\log_{10}$ ratio of the CEST effects from two labile protons on the same contrast agent is linearly correlated with pH[13] and independent of concentration, endogenous T_1 relaxation time, and incomplete saturation.[14–15]

The goal of this work was to optimize the CEST MRI technique for an orthotopic model of ovarian cancer. MRI of the intraperitoneal region suffers from significant motion artifacts due to respiratory motion. Respiration gating is a common means to deal with these types of motion artifacts. A gated CEST protocol was previously developed by our group,[16] but this protocol suffered from incomplete saturation due to a variable time delay between the end of the saturation pulse and the beginning of FISP acquisition. Therefore, an improved respiration gated CEST protocol that had no delay between saturation and acquisition was implemented. In addition, we used an improved data fitting technique to measure pHe. Past acidoCEST MRI studies have used Lorentzian line fitting to measure pHe.[17] However, Lorentzian line fitting requires 3 different parameters per peak to be fit to generate pH values, thus increasing the likelihood of erroneous results due to over-fitting, which is especially problematic at neutral pH environments where the amplitude of the CEST peak of one of the exchangeable protons of iopamidol is especially low. Bloch fitting fits for pH directly and is therefore less likely to over-fit the CEST MRI results.

2. MATERIALS AND METHODS

2.1 Mouse Model

Mouse Model—All *in vivo* studies with tumor models were performed with the approval of the Institutional Animal Care and Use Committee of the University of Arizona. To prepare the mouse model with a flank tumor, ten female C.B-17/ICRACC white SCID mice, aged 4–8 weeks old, were inoculated subcutaneously with 1 million tumor cells of a SKOV3 tumor cell line in 0.5 mL of 50% matrigel. Mice were imaged weekly for five weeks with the first time point being two weeks after inoculation. Tumors were 50 – 150 mm^3 at the first time point and 350 – 750 mm^3 at the final time point. All mice survived throughout the study but there was not always sufficient uptake of the agent into the flank tumors to allow for pH measurements. To prepare the mouse model with an orthotopic tumor, eight female C.B-17/ICRACC white SCID mice, aged 4–8 weeks old, were inoculated i.p. with 1 million tumor cells of a SKOV3 tumor cell line in 0.5 mL of 50% matrigel of a SKOV3 tumor cell line. Mice were imaged weekly for four weeks with the first time point being three weeks after inoculation. Tumors were 30 – 50 mm^3 at the first time point and 150 – 200 mm^3 at the final time point. One mouse died before the study began and four more died by the final time point. Additionally, pH measurements were not able to be determined for some mice at certain time points due to insufficient uptake of the agent or the inability to distinguish the tumor from the healthy tissue. Each mouse was euthanized after the last imaging scan.

2.2 In *Vivo* MRI Studies

Mouse Preparation—To prepare for each MRI study, a mouse was anesthetized with 1.5–2.5% isoflurane gas anesthetic delivered in 1 L/min oxygen gas ventilation, and secured to a mouse cradle. A rectal probe to monitor temperature and a respiration pad to monitor respiration rate were connected to the mouse, and a catheter was inserted into the tail vein to deliver the contrast agent. Core body temperature of the mouse was maintained throughout the imaging experiment at 37. ± 0.5°C using an automated feedback loop between the temperature probe and an air heater (SA Instruments, Inc., Stony Brook, NY).

For the flank model, we performed four pre-injection acidoCEST MRI scans before injection of the contrast agent, and six post-injection scans after injection of the contrast agent. The differences between these scans removed endogenous CEST effects from the analysis of tumor pHe. Endogenous CEST effects are particularly problematic to pH analysis when the CEST signal amplitude from the agent is similar in amplitude to the CEST signal amplitude from endogenous molecules. This was the case for the flank model, which only received i.v. delivery and infusion of the agent. We extended a catheter line from the inner bore of the magnet to the outside working space to ensure that we did not need to displace the mouse between the pre-injection and post-injection scans. Upon completion of the last pre-injection scan, a bolus of 50 μL of saline "dead volume" followed by 200 μL of iopamidol at 370 mgI/mL concentration was injected i.v. via the catheter, for a total of 250 μL of injection volume. The catheter was then connected to an infusion pump, and iopamidol was delivered at 400 μL/hr throughout the post scan. The post-injection scans were then acquired.

For the orthotopic model, initial studies showed that administration of the agent solely by i.v. injection followed by infusion delivered an insufficient concentration of the agent to the tumor area to allow for adequate CEST detection. We therefore injected a 400 μL bolus of the agent at 370 mgI/ml concentration into the i.p. cavity of the mouse before placing the mouse into the MRI scanner. We also infused the agent i.v. at 400 μL/hr throughout the imaging session. As a result of this different delivery method, we did not perform a pre-injection scan, so our CEST spectrum contained endogenous CEST effects in addition to the

CEST effects of our agent. Fortunately, injecting the agent i.p. delivered a much higher concentration of the agent to the tumor than delivery to the flank model. The i.p. injection resulted in a much larger CEST signal from our agent than endogenous CEST signals thereby improving the identification of our agent's CEST signals during subsequent analyses.

MRI of the Flank Tumor Model—A multi-slice, spin echo MRI protocol without respiration gating was used to identify and measure tumor volumes of the flank model. Images were acquired with a 1075.6 ms TR; 12.7 ms TE; 1 mm slice thickness; 10 contiguous axial slices; 453 × 453 μm^2 in-plane resolution; 128 × 128 matrix size; 5.8 cm^2 field of view; 1 average. The total acquisition scan time was 2:17 min. We used an ungated acidoCEST MRI pulse sequence for imaging the flank tumor model because flank tumors are not susceptible to motion. Our ungated method used a single half gauss saturation pulse at 3.5 μT power and 0.3 Hz bandwidth for 5 s. After each saturation pulse a FISP sequence was used to acquire an MR image. The FISP MRI protocol used a 3.70 ms TR; 1.60 ms TE; 10° excitation angle; 1.0 mm slice thickness; 453 × 453 μm^2 in-plane resolution; 128 × 128 matrix size, 5.80 cm^2 field of view; axial orientation; centric encoding, and 1 average. The FISP scan time was 419 ms. This sequence was repeated with a series of 40 saturation frequencies to acquire a CEST spectrum in 3:47 min. This method was repeated 4 times for the pre-injection scan and 6 times for the post-injection scan. The total scan time for the pre-injection and post-injection scans was 37:50 min.

MRI of the Orthotopic Tumor Model—A multi-slice, multi-echo MRI protocol with respiratory gating was performed to identify and measure tumor volumes of the orthotopic model. Images were acquired with a 1.763 s TR; 10.6, 21.3, 31.9, 42.5, 53.2 and 63.8 ms TEs; 1 mm slice thickness; 12 contiguous coronal slices; 453 × 453 μm^2 in-plane resolution, 128 × 128 matrix size, 5.8 cm^2 field of view; 2 averages. The total acquisition scan time was 7:31 min. The echo acquired with a 21.3 millisecond TE had the best contrast for identifying the tumor.

The tumors in the orthotopic tumor model were found in the intraperitoneal cavity, often immediately distal to the liver. As a result, a respiration gated sequence had to be used to avoid motion artifacts that would corrupt data analysis. Respiration gating in MRI is commonly practiced by triggering the start of the pulse sequence soon after the end of exhalation. However, the long duration of the saturation period in CEST MRI exceeds the time for one breath, which is typically less than 1.5 seconds at 40 breaths per minute under anesthesia. This long saturation period would cause the FISP acquisition to no longer be synchronized with lung motion.

To avoid this problem, we redesigned our acidoCEST MRI method to avoid FISP acquisition during mouse respiration (Fig. 1). We applied ten continuous wave saturation pulses each 600 ms long for a total minimum length of 6 s for the saturation period. Each pulse was applied at 3.5 μT power and 2.1 Hz bandwidth. Immediately after this train of pulses, we programmed the sequence to check if the respiration trigger was active. We set the trigger to be active in a region of 350 to 1000 ms after the last breath, which served as an optimal time period in between breaths where there was no chance of motion due to lung movement. If the trigger was active, then the sequence would immediately begin FISP imaging. If the trigger was not active, then the sequence would produce one saturation pulse for 600 ms and then recheck if the trigger was active. This process would repeat until the trigger was active and FISP imaging could occur. In practice, this procedure acquired a FISP image after 6.0, 6.6, or 7.2 s of saturation. Except for using a coronal image orientation, FISP imaging for the orthotopic tumor model was the same as FISP imaging for the flank model. The sequence was repeated with a series of 40 saturation frequencies to acquire a CEST spectrum. The time to acquire each CEST spectrum was 5 to 6 minutes, which fluctuated because the saturation pulse length for each data point depended on the mouse breathing pattern and rate. The gated CEST MRI protocol was repeated for 4 scans, making the total scan time 20 to 24 minutes long.

Six seconds was chosen as a minimum length for our MRI saturation pulse to ensure that steady state magnetization in the presence of saturation was close to fully established before the next FISP MRI acquisition. Ensuring steady state magnetization in the presence of saturation for each MRI acquisition was critical because the length of the saturation period was not constant due to respiration gating. It has been shown in past work that the CEST signal increases from 16.64% to 17.44% with a saturation time of 6.0 to 7.2 seconds for the 5.6 ppm peak of iopamidol, and from 20.09 to 21.06% for the 4.2 ppm peak of iopamidol. Although this change may be seen as potentially significant, this equates to a difference in a calculated pH value of only 0.0016.

2.3 Image Analysis

Tumor Volumes—The tumor volumes were determined from manually selected regions of interest from the anatomical MR images. Tumor volumes were calculated by summing the areas of the lesion in each slice using ImageJ.

Phantom Analysis for base catalyzed exchange rate calculations—Phantoms of Iopamidol were prepared at 78 mM at pH values of 5.82, 6.08, 6.47, 6.72, 6.93, 7.42 and 7.67. An additional phantom was prepared at 39 mM with a pH value of 6.72. Phantoms were warmed to 37 degrees with hot air in a Bruker 600 MHZ vertical bore spectrometer. Data was acquired using the high throughput CEST technique. In order to mitigate effects of diffusion, three high throughput techniques were used per phantom, collecting data from −7.5 ppm to 0 ppm, −2.5 to 5 ppm, and 2.5 ppm to 10 ppm in 0.03 ppm increments. The overlap of the data was to confirm that the contrast from phantoms did not change between experiments. The region used to fit phantoms was from −5 to 10 ppm with a step size of 0.03 ppm increments.

pH Analysis of the Flank tumor model—The images generated from the four pre-injection MRI acquisitions and were averaged and spatially smoothed with Gaussian filtering (Fig. 2). Images from the six post-injection MRI acquisitions were also averaged and spatially smoothed. A CEST spectrum was constructed for each pixel for the averaged pre-injection and post-injection scans. The pre-injection spectrum was subtracted from the post-injection spectrum to remove endogenous CEST effects. The pH was determined by parameterizing the contrast of the exogenous agent with respect to pH via the Bloch equations modified for chemical exchange (Fig. 3A). The step size used was 10^{-8} and the function tolerance set to 10^{-8}. The base catalyzed exchange rates were calibrated by fitting phantoms using the Bloch equations. The exchange rate was determined as a function of pH and base catalyzed exchange rate. This enabled us to fit pH directly in our model instead of individually fitting exchange rates for all labile pools. The parameters used to fit were pH (initial guess = 7.0), concentration (initial guess = 10 mM), T_1 relaxation time constant of water (initial guess = 2.0 sec), T_2 relaxation time constant of water (initial guess = 0.056 sec), B_0 offset (initial guess = 360 Hz), and a scale factor to account for the baseline changing between the pre-injection and post-injection scans (initial guess = 1 We optimized the initial guesses empirically.

pH Analysis of the Orthotopic tumor Model—The images generated from the four CEST-FISP MRI acquisitions were averaged and smoothed with Gaussian filtering. A CEST spectrum was constructed for each pixel and was fit with Bloch equations. The CEST signals from endogenous molecules were broad due to the high saturation power that was used during the study. These endogenous CEST signals were low relative to the high CEST signals from the agent. Therefore, the endogenous CEST signals could not be distinguished within the CEST spectrum and were not fit as a separate feature during Bloch fitting. This high concentration allowed for Bloch fitting of the Z spectrum after agent injection to be successful in determining pH without the need for the pre-injection images. Initial guesses for the parameters used for fitting were: T_1 = 2.0 sec, T_2 = 0.020 sec, 50 mM concentration, B_0 shift = 360 Hz, scale factor = 1 and pH = 7.0. We optimized the initial guesses empirically to generate the best fits to the data.

2.4 pH Analysis

The average pH of the tumor for a specific mouse was determined from the average value of all the pH measurements for the pixels that represented the tumor. We set a pH value of 7.4 as the threshold for acceptable pH measurements. Any imaging data that produced an average pH value of 7.4 or higher were discarded from analysis. We similarly discarded any imaging data that gave an average concentration of 80 mM or higher from analysis. This was done to prevent including analysis of a bolus residue into the results, which, like the tumors, appeared as a bright spot in the T_2 weighted sequence. Two mice showed pH measurements of 7.4 or higher and 2 mice showed concentration measurements of 80 mM or higher. The results of these 4 mice were excluded from the correlation plots.

3. RESULTS

3.1 Respiration Gated acidoCEST-MRI

We implemented respiration gating into our acidoCEST MRI pulse sequence when imaging the orthotopic model to reduce motion artifacts that could confound results. The gated pulse sequence was a modified version of a previous gated sequence that we used to image fibrotic lesions in an idiopathic pulmonary fibrosis (IPF) mouse model.[16] The major strength of the old sequence was that FISP acquisition would not occur during respiration. This was accomplished by placing the trigger between the saturation pulse and FISP acquisition. Unfortunately, the old sequence had the length of the saturation pulse set to a fixed time so that there would inevitably be CEST decay between the end of the saturation pulse and the beginning of FISP acquisition due to variability in mouse breathing rates and patterns.

In this study we modified the sequence to be adaptive to the mouse respiration rate and the time at which the sequence began relative to the mouse respiration pattern so that there would be no CEST decay between the end of the saturation pulse and the beginning of FISP acquisition. This was accomplished by using multiple short rectangular pulses for the saturation pulse and incorporating the trigger within this saturation sequence. A fixed length of rectangular pulses was used initially to ensure CEST steady state had been reached. After this, each subsequent rectangular pulse that was started would be immediately followed to determine if the trigger was active. If it was active, FISP acquisition would immediately occur. If it was not active, another rectangular saturation pulse would start and the process would continue. As demonstrated in Figure 1, this procedure ensured that there was no delay in between the end of the saturation pulse and the beginning of FISP acquisition even if the start of the pulse sequence and the respiration pattern of the mouse changed relative to one another.

3.2 acidoCEST Data Analysis

Experience with past acidoCEST MRI studies has shown that injection of the contrast agent i.v. often results in poor uptake by flank tumor models. As a result, it is occasionally difficult to be certain that the detected CEST contrast is due to the agent or endogenous molecules like APT that have similar MR frequencies to the agent. To avoid this problem, we included four scans prior to agent injection (pre-scans) in addition to six scans after agent injection (post-scans) with the flank tumor model. We then could subtract the signal intensities generated in the post-scan from the pre-scan with the hope that any endogenous CEST effects would be removed (Figure 2). Before generating this difference spectrum (pre-post), we averaged the collection of pre-scans and the collection of post-scans to generate an average pre-scan and an average post-scan to increase SNR. We also performed a Gaussian filter on both of the averaged scans to further increase SNR. We subsequently obtained the difference of these two images to generate a difference image, which is the image that we used to determine pH.

3.3 acidoCEST Data Fitting

Once generating a spectrum with our difference image, we chose to perform Bloch fitting instead of Lorentzian line fitting with the data to generate pHe values. We did this specifically because past experience with data fitting *in vivo* CEST spectra has shown that Lorentzian line fitting is susceptible to over-fitting into noisy spectra as demonstrated in Figure 3B. Conversely, Bloch fitting is not susceptible to over-fitting (Figure 3A). Additionally, Bloch fitting uses 7 parameters, which are fewer than the 9 required for Lorentzian line shape fitting thus offering another advantage.

Bloch fitting includes concentration as a parameter for fitting, which gives an added benefit of generating an additional biomarker that we can measure with acidoCEST MRI. The concentration of the agent within the tumor may provide an indication of the vascularity of tumor models.

3.4 Parametric Maps of Flank and Orthotopic Tumor Model

Representative pHe maps of a flank tumor (Figure 4A) and an orthotopic tumor (Figure 4B) showed heterogeneous pHe values within the tumor. This was a consistent result between both the orthotopic and flank tumor models. Additionally, the large amount of colored pixels within both tumor models indicates that the majority of pixels had good fits, demonstrating that our acidoCEST technique performed well in both models. Lastly, the flank tumor appears to be much larger than the orthotopic tumor. Flank tumors in general were larger than the orthotopic tumors especially by the end of the study. Although each study was imaged for the same amount of time, the orthotopic tumors grew slower than the flank tumors.

3.4 acidoCEST MRI of Flank and Orthotopic Tumor Model

The flank tumor model showed a decrease in pHe as the tumor volume increased, which supports the idea that as tumors increase in size, they become more metabolically active. Surprisingly, the orthotopic tumor model showed no relationship between pHe and tumor volume. Notably, the orthotopic tumors never grew to the same size as the flank tumors due to a slower growth rate. For instance, the largest orthotopic tumor measured was slightly over 200 mm^3 whereas the largest flank tumor was over 750 mm^3. A slow growth rate may explain why tumor pHe did not decrease over time for the orthotopic model. Neither tumor model showed a relationship between concentration and tumor volume suggesting that the size of the tumor had no impact on the uptake of iopamidol into the tumor microenvironment.

4. DISCUSSION

We have developed a novel respiration gated CEST MRI protocol that can accurately measure pHe in orthotopic ovarian tumors. This protocol relies on a long CEST saturation pulse followed by short CEST saturation pulses if needed. The short CEST saturation pulses occur if the trigger is not active after the long CEST saturation pulse has fired, where an active trigger is defined by the user to be a time range when the mouse is not breathing. If the trigger is active, then FISP acquisition occurs. This pulse sequence design ensures that there is no CEST decay in between the saturation pulse and FISP acquisition and that FISP acquisition occurs when the mouse is relatively motionless, thus resulting in accurate pHe measurements.

We have also developed a novel image data fitting procedure using the Bloch equations modified for chemical exchange. The inclusion of pre- and post- injection CEST scans enables us to generate a difference spectrum that eliminates endogenous CEST effects like APT that have similar resonance frequencies as iopamidol. This ensures that the CEST peaks that we are fitting to determine pHe are truly due to our exogenous agent. Additionally, using the Bloch equations modified for chemical exchange to fit the CEST peaks has been shown to be less susceptible to over-fitting as compared to Lorentzian line fitting, which was used by our group in the past. Bloch fitting will be especially advantageous as we move from small animal imaging at 7T to clinical imaging at 3T because the two CEST signals from iopamidol will be more likely to overlap at lower magnetic field strengths. This will further increase the chance of inaccurate pHe measurements with Lorentzian line fitting since the percentage of pixels that could suffer from over-fitting errors will be greater.

This study combined the measurements of pHe and concentration of agent in flank and orthotopic tumors with CEST MRI, with the tumor volume measured with T_2-weighted MRI. The ability to measure three biomarkers within one scan session provided an efficient evaluation of both tumor models. Additionally, comparing these three biomarkers between the flank and orthotopic models gives insight into differences in the microenvironment of a tumor depending on its location.

The pHe measurements with acidoCEST MRI suggested that larger flank tumors produced more lactic acid than smaller flank tumors. There was not a similar trend seen in the orthotopic model. Notably, the flank tumor model grew faster than the orthotopic tumor model. A past acidoCEST study indicated a correlation between tumor growth rate and pHe, suggesting that pHe indicates the rate of glycolytic tumor metabolism.[10] The slow tumor growth rate and steady pHe measurements in the orthotopic tumor model suggest that tumor metabolism is steadier than the flank tumor model. The concentration results show no difference between large and small tumors of either the flank and orthotopic tumor models. Concentration is related to vascular permeability and vascular flow, so these results suggest that both the flank and orthotopic tumor models show a similar combination of permeability and blood flow in the tumor.

Future studies could assess the relationship between *in vivo* pHe measurements relative to *ex vivo* analyses of pH related biomarkers, like hypoxia, for additional biomarker comparisons. In addition, future clinical acidoCEST studies targeting tumors in the i.p. or lung region could use the respiration gated pulse sequence described in this paper to improve pHe measurements. Imaging flank tumors is not an option in the clinic so motion will be a more common issue in future clinical projects as compared to past pre-clinical projects. Finally, Bloch fitting to generate pHe from acidoCEST data will be advantageous at 3T magnetic field strength because the two CEST signals from iopamidol will be more likely to overlap and and less agent will be injected into patients relative to body weight so the CEST signals will be smaller.

5. CONCLUSION

Respiration gated acidoCEST MRI measured pHe in an orthotopic tumor model and flank tumor model. There was a negative correlation seen between tumor volume and tumor pHe in the flank tumor model, but no correlation seen in the orthotopic tumor model. This suggests that tumor metabolism is steadier for the orthotopic tumor model. Bloch fitting proved to be less subject to over fitting errors than Lorentzian line fitting. This result will become more impactful as CEST MRI is translated to clinical scanners at lower magnetic field strengths because the two CEST signals from iopamidol will be more likely to overlap.

References

1. Vazquez A, Jiangxia L, Yi Z, Zoltán NO. Catabolic Efficiency of Aerobic Glycolysis: The Warburg Effect Revisited. BMC Systems Biology BMC Syst Biol. 2010; 4:1. [PubMed: 20056001]
2. Raghunand N, Gatenby RA, Gillies RJ. Microenvironmental and cellularconsequences of altered blood flow in tumours. Br J Radiol. 2003
3. Gatenby RA, Gawlinski ET, Gmitro AF, Kaylor B, Gillies RJ. Acid mediated tumor invasion: a multidisciplinary study. Cancer Res. 2006
4. Estrella V, Chen T, Lloyd M. Acidity generated by the tumor microenvironment drives local invasion. Cancer Res. 2013
5. Arcamone F, Franceschi G, Penco S, Selvia A. Adriamycin 14-hydroxydaunomycin: a novel antitumor antibiotic. Tetrahedron Lett. 1969
6. Raghunand N, Gillies RJ. pH and drug resistance in tumors. Drug Resist Updates. 2002
7. Mahoney BP, Raghunand N, Baggett B, Gillies RJ. Acid pH affects the distribution of chemotherapeutic agents in vitro. Biochem Pharmacol. 2003
8. Raghunand N, Mahoney BP, Gillies RJ. pH-dependent partition coefficients predict importance of ion trapping on pharmacokinetics of weakly basic chemotherapeutic agents. Biochem Pharmacol. 2003
9. Robey IF, Baggett BK, Kirkpatrick ND. Bicarbonate increases tumor pH and inhibits spontaneous metastases. Cancer Res. 2009
10. Chen LQ, Howison CM, Jeffery JJ. Evaluations of extracellular pH within In Vivo Tumors Using acidoCEST MRI. Magn Reson Med. 2013
11. Aime S, Calabi L, Biondi L. Iopamidol: exploring the potential use of a well-established x ray contrast agent for MRI. 2005
12. Liepinsh E, Otting G. Proton exchange rates from amino acid side chains—implications for image contrast. Magn Reson Med. 1996
13. Sheth VR, Li Y, Chen LQ. Measuring in vivo tumor pHe with CEST-FISP MRI. Magn Reson Med. 2012
14. Liu G, Li Y, Sheth VR, Pagel MD. Imaging in vivo extracellular pH with a single PARACEST MRI contrast agent. Mol Imaging. 2012
15. Sheth VR, Li Y, Chen LQ, Howison CM, Flask CA, Pagel MD. Measuring in vivo tumor pHe with CEST-FISP MRI. Magn Reson Med. 2012
16. Jones KM, Randtke ER, Howison CM, Cardenas-Rodriguez J, Kottmann MR, Pagel MD. Measuring Extracellular pH in a Lung Fibrosis Model with acidoCEST MRI. Molecular Imaging and Biology. 2014
17. Sheth VR, Liu G, Li Y, Pagel MD. Improved pH measurements with a single PARACEST MRI contrast agent. Contrast Media Mol Imaging. 2012

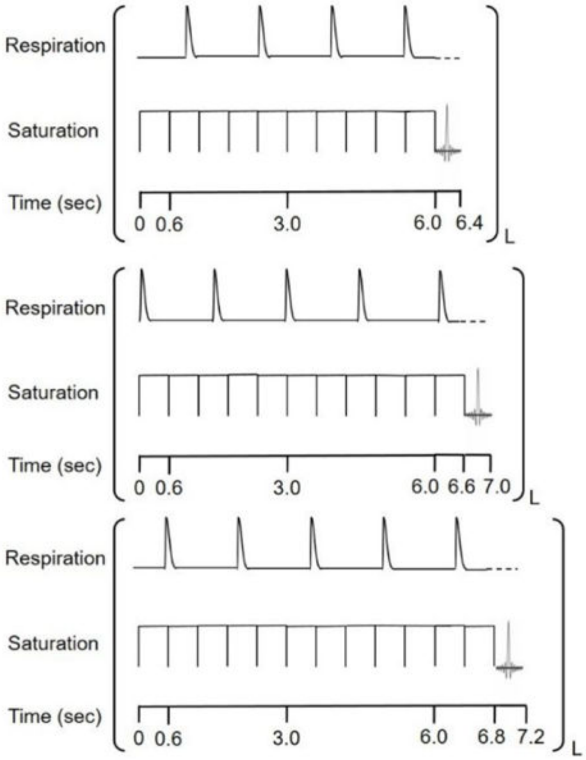

Figure 1.

Respiration gated CEST pulse sequence. A fixed set of 10 rectangular pulses, each 600 milliseconds long, was used before each acquisition to ensure that CEST steady state had been reached. If the trigger was active (300–600 milliseconds after a respiration) as is the case for the top figure, FISP acquisition would immediately occur. If the trigger was not active, as is the case for the bottom two figures, another 600 millisecond rectangular pulse would start and then again there would be a check to determine if the trigger was active. This sequence setup ensured there was no gap in between the end of the CEST pulse and the beginning of FISP acquisition. An active trigger is indicated with a dash line for respiration and L indicates the offset frequency for the CEST pulse. This sequence would be repeated for multiple offsets to generate a CEST spectrum.

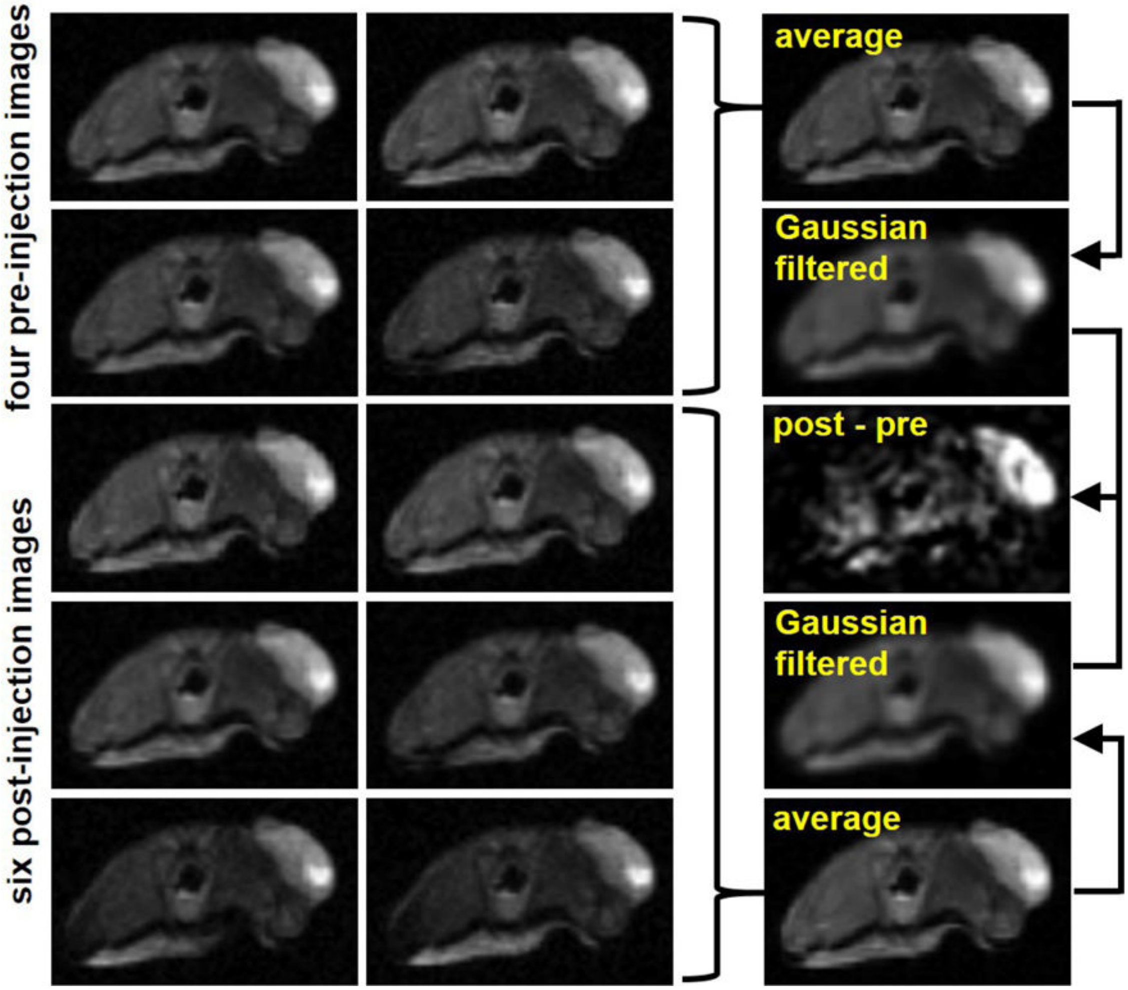

Figure 2.

An outline of CEST image processing. The four pre-injection scans acquired are averaged and then a Gaussian filter is performed. The same process is performed with the six post-injection scans. The average post-injection scan is subtracted from the average pre-injection scan. The CEST spectrum from the remaining difference (post-pre) image is fit to generate pHe of the tumor.

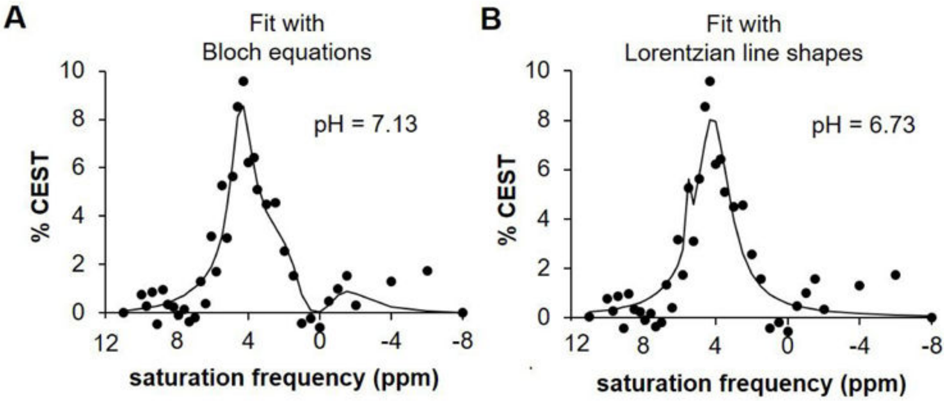

Figure 3.

A comparison of A) Bloch fitting and B) Lorentzian line fitting in a pixel with a neutral pH. Lack of a clear peak at 5.6 leads to overfitting with Lorentzian line fitting, thus resulting in an error in pH measurement. Bloch fitting is not susceptible to this error.

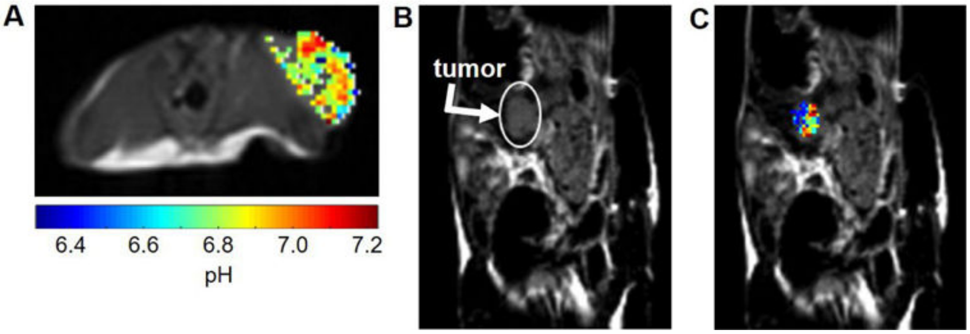

Figure 4.

Representative pHe maps of A) flank and B) C) orthotopic tumor models show heterogeneous pHe measurements throughout the tumor

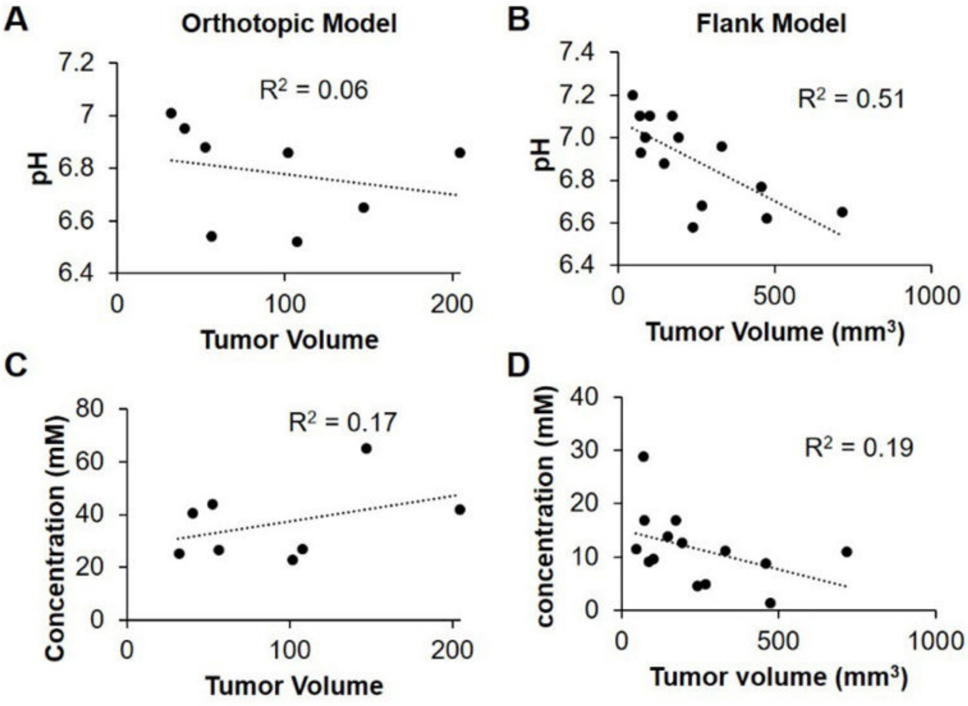

Figure 5.

Trends in A,B) pH and C,D) concentration vs. tumor volume in both the A,C) orthotopic and B,D) flank tumor models.